

# Measurement of the $^{159}\text{Tb}(\text{n}, \gamma)$ cross section at the CSNS Back-n facility

S. Zhang,<sup>1,\*</sup> G. Li,<sup>1</sup> W. Jiang,<sup>2</sup> D.X. Wang,<sup>1</sup> J. Ren,<sup>3</sup> M. Huang,<sup>1,†</sup> E.T. Li,<sup>4</sup> J.Y. Tang,<sup>2</sup> X.C. Ruan,<sup>3</sup> H.W. Wang,<sup>5</sup> Z.H. Li,<sup>3</sup> Y.S. Chen,<sup>3</sup> L.X. Liu,<sup>5</sup> X.X. Li,<sup>6</sup> Q.W. Fan,<sup>3</sup> R.R. Fan,<sup>2</sup> X.R. Hu,<sup>6</sup> J.C. Wang,<sup>1,3</sup> X. Li,<sup>1</sup> D.D. Niu,<sup>1</sup> N. Song,<sup>1,3</sup> and M. Gu<sup>1</sup>

<sup>1</sup>College of Mathematics and Physics, Inner Mongolia Minzu University, Tongliao 028000, China.

<sup>2</sup>Institute of High Energy Physics, Chinese Academy of Sciences, Beijing 100049, China.

<sup>3</sup>China Institute of Atomic Energy, Beijing 102413, China.

<sup>4</sup>Institute for Advanced Study in Nuclear Energy & Safety,

College of Physics and Optoelectronic Engineering, Shenzhen University, Shenzhen 518060, China.

<sup>5</sup>Shanghai Advanced Research Institute, Chinese Academy of Sciences, Shanghai 201210, China.

<sup>6</sup>Shanghai Institute Applied Physics, Chinese Academy of Sciences, Shanghai 201800, China.

The stellar ( $\text{n}, \gamma$ ) cross section data for the mass numbers around  $A \approx 160$  are of key importance to nucleosynthesis in the main component of the slow neutron capture process, which occurs in the thermally pulsing asymptotic giant branch (TP-AGB). The new measurement of ( $\text{n}, \gamma$ ) cross sections for  $^{159}\text{Tb}$  was performed using the C<sub>6</sub>D<sub>6</sub> detector system at the back streaming white neutron beam line (Back-n) of the China spallation neutron source (CSNS) with neutron energies ranging from 1 eV to 1 MeV. Experimental resonance capture kernels are reported up to 1.2 keV neutron energy with this capture measurement. Maxwellian-averaged cross sections (MACS) are derived from the measured  $^{159}\text{Tb}$  ( $\text{n}, \gamma$ ) cross sections at  $kT = 5\text{--}100$  keV and are in good agreement with the recommended data of KADoNiS-v0.3 and JEFF-3.3, while KADoNiS-v1.0 and ENDF-VIII.0 significantly overestimate the present MACS up to 40% and 20%, respectively. A sensitive test of the s-process nucleosynthesis is also performed with the stellar evolution code MESA. Significant changes in abundances around  $A \approx 160$  are observed between the ENDF/B-VIII.0 and present measured rate of  $^{159}\text{Tb}(\text{n}, \gamma)^{160}\text{Tb}$  in the MESA simulation.

PACS numbers: 25.70.Pq

Keywords:

## I. INTRODUCTION

The elements heavier than iron in the solar system are mainly produced by the slow neutron capture process (s-process) [1] and the rapid neutron capture process (r-process) [2] in stars as found by Burbidge et al. [3] and Cameron [4] as early as in 1957. Almost less than 1% of heavy elements are ascribed to the production of photo-disintegration processes (the so-called p/ $\gamma$  process), neutrinos, and charged-particle induced reactions [5, 6]. The s-process takes place during stellar evolution and path through nuclei along the valley of  $\beta$  stability with lower neutron densities and temperatures. The weak s-process is responsible for producing isotopes up to  $A \approx 90$  and occurs during He and C burning in massive stars. While the main s-process contributes isotopes  $A \approx 90\text{--}208$  and take place in the thermally pulsing asymptotic giant branch (TP-AGB) phase of low- and intermediate-mass stars. The r-process is related to explosive nucleosynthesis in massive stars and binary star mergers with relatively high neutron densities.

Terbium is mainly produced by the explosive r-process [2], while about 9% is made by main s-process in low- and intermediate-mass TP-AGB stars [7]. The s-process reaction path around terbium is sketched in Fig. 1.  $^{160}\text{Tb}$  is an important s-process branching point, which is shielded against the  $\beta^-$  decay chains from the r-process by stable nuclei  $^{160}\text{Gd}$ . The abundance of  $^{160}\text{Tb}$  will affect the s-only isotope  $^{160}\text{Dy}$ , which paths through the s-process to  $^{161}\text{Dy}$  and considered as an reference point for the reaction flow. Also, neutron capture of terbium isotopes will contribute to the production of p-nuclei  $^{164}\text{Er}$  through the temperature sensitive branching at  $^{163}\text{Dy}$  to  $^{163}\text{Ho}$  by the nuclear reaction path  $^{163}\text{Ho}(\text{n}, \gamma)^{164}\text{Ho}(\beta)^{164}\text{Er}$  in the stellar environment [8–10].

Two groups of experimental neutron capture cross section data for  $^{159}\text{Tb}(\text{n}, \gamma)$  reaction were reported between 1961 and 1991 [11–16] in the astrophysical interested energy region. Data from Block et al. [11], Gibbons et al. [12], Lépine et al. [13] are significantly larger than data of Mizumoto et al. [14], Ohkubo et al. [15] and Bokhovko et al. [16]. In the KADoNiS-v0.3 [17] database, the recommended Maxwellian-averaged cross sections (MACS) of  $^{159}\text{Tb}(\text{n}, \gamma)$  at stellar temperature  $kT = 30$  keV is  $1580 \pm 150$  mb, which is widely used in stellar nucleosynthesis calculations, derived from the neutron capture cross section data of Mizumoto et al. [14] and Bokhovko et al. [16]. While, this value reported by the recent activation measurement [18] with  $2166 \pm 181$  mb and it varies from 1116 to 2949 mb in the collection list of the KADoNiS-v1.0 [19] and references therein. Because of so large discrepancies, newer measurements of stellar neutron capture cross section of  $^{159}\text{Tb}$  are desired for improving the reliability of recommended data. Much higher accurate neutron capture cross sections for the terbium isotopes are required to the s-process nucleosynthesis, and the

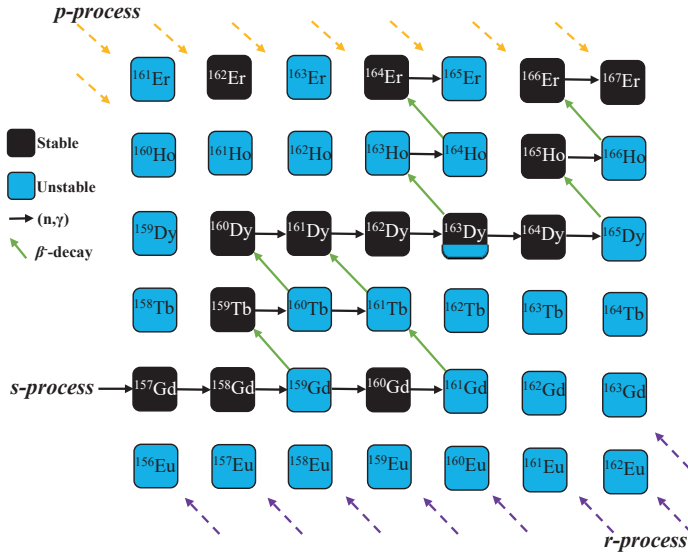


FIG. 1: (color online) The s-process reaction path in the region of terbium. Black solid boxes indicate stable; blue empty boxes indicate unstable isotopes. Arrows to the right and the next higher elements represent neutron capture reactions and  $\beta^-$  decays, respectively. The isotope  $^{163}\text{Dy}$  is a terrestrially stable nucleus, which becomes unstable at stellar temperature [8].

separation of the r and s components in the observed Tb abundance through subtraction of the s abundances from the respective solar values. In addition, the  $^{159}\text{Tb}(n, \gamma)$  cross section data is very important for the design of nuclear reactor and the research in nuclear structure [20, 21].

In the past years, a series of neutron radiative capture experiments have been performed using the  $\text{C}_6\text{D}_6$  detectors with the total energy technique [22–26] and the total absorption calorimeter consists of  $\text{BaF}_2$  scintillator arrays [27–30] in combination with the  $^7\text{Li}(p, n)^7\text{Be}$  reaction neutrons and white neutron sources. Both of the  $\text{C}_6\text{D}_6$  and  $\text{BaF}_2$  detection systems, respectively, were constructed at the back streaming white neutron facility (Back-n) of the China Spallation Neutron Source(CSNS) [31, 32], which is the only high intense pulsed spallation reaction neutron source in China at present. The main physics motivation of these systems is to measure the neutron capture data related to the nuclear astrophysics, advanced nuclear energy technologies such as accelerator-driven subcritical systems, thorium-based molten salt reactor, and fourth generation reactors. The detection systems, experimental techniques, background study and resonance energy region measurements have been described in Refs [33–36]. In this work, we report the new experiment of neutron capture cross sections for  $^{159}\text{Tb}$  over the energy range from 1 eV to 1 MeV via the time-of-flight (TOF) method combined with the white neutron beam at the CSNS Back-n facility. The resonance kernels of  $^{159}\text{Tb}(n, \gamma)$  are obtained up to 1.2 keV, and the MACS for the astrophysical interest energy region from  $kT = 5\text{--}100$  keV are calculated.

## II. EXPERIMENT

The measurement of the  $^{159}\text{Tb}(n, \gamma)$  was performed at the CSNS Back-n facility [31, 32] in China. Neutrons were produced via the spallation reactions by bombarding a massive tungsten target with a 1.6 GeV proton beam, operating at a 25 Hz repetition rate and collimated to a 30 mm diameter beam spot at the sample position. The neutron energies ranging from thermal to a few hundred MeV were determined using the time of flight (TOF) method with a 76 m long flight path. The neutron capture yields were studied using the total energy measurement principle based on an array of four  $\text{C}_6\text{D}_6$  detectors with the pulse height weighting techniques (PHWT) [37–39]. The neutron flux in the energy range of 1 eV to 100 MeV was obtained with a combination of the data from dedicated measurements of the  $^6\text{LiF}$ -silicon (Li-Si) detector array [40] and the  $^{235}\text{U}$  loaded multilayer fission chamber [41]. The Li-Si detector neutron flux was normalized to  $^{235}\text{U}$  data at 10–20 keV since its position was about 20 m away from the sample. The samples used for this experiment are listed in Table I. A metallic terbium sample of natural abundance with a thickness of 0.2 mm was used for the  $^{159}\text{Tb}(n, \gamma)$  reaction study. The  $^{197}\text{Au}$  sample was used as the standard for calculating the relative cross section of  $^{159}\text{Tb}(n, \gamma)$  in neutron energies ranging from 2 keV to 1 MeV. The  $^{nat}\text{Pb}$  samples were used to normalize the neutron fluence and to evaluate the in-beam  $\gamma$ -rays and scattered-neutron backgrounds, respectively.

The empty sample runs were also performed to evaluate the background produced from the upstream devices, such as the sample holders, etc. All experimental data were collected on an event-by-event basis high-performance data acquisition system with a 12-bit full-waveform digitizers sampling at 1 GS/s [42]. The offline data analysis was done on the CERN ROOT framework [43].

TABLE I: Characteristic parameters of samples

Sample	Thickness (mm)	Diameter (mm)	Mass (mg)	Area desity ( $atom \cdot b^{-1}$ )
$^{nat}Tb$	0.20	30	1169.14	$6.27 \times 10^{-4}$
$^{197}Au$	0.10	30	1357.17	$5.87 \times 10^{-4}$
$^{nat}Pb$	0.53	30	4249.75	$1.75 \times 10^{-3}$
Empty holder				

### III. DATA ANALYSIS AND RESULTS

The incident neutron energy  $E_n$  was determined by employing the TOF method through the nonrelativistic kinematics formula (1). The neutron effective flight path  $L$  was obtained by analyzing the low energy resonances of the gold sample.

$$E_n = \left( \frac{72.2977 \times L}{t_n} \right)^2 \quad (1)$$

where  $E_n$  is in MeV,  $L$  is in meters, and  $t_n$  is the flight time in ns.

The experimental neutron capture yield as a function of  $E_n$  can be calculated as:

$$Y_{exp}(E_n) = \frac{1}{f} \frac{C^w(E_n) - B^w(E_n)}{\Phi(E_n) \times E_c} \quad (2)$$

where  $f$  is the normalization factor determined by self-normalizing the measured capture yield of 4.9 eV resonance of  $^{197}Au$  and 11.1 eV resonance of  $^{159}Tb$ , based on the saturated resonance technique [44, 45].  $E_c$  is the detection efficiency for a capture event,  $\Phi(E_n)$  is the neutron flux spectrum, and  $C^w(E_n)$  and  $B^w(E_n)$  are the weighted count spectrum and the total background spectrum, respectively.

The PHWT method is essential for the  $(n, \gamma)$  cross section measurement using the C<sub>6</sub>D<sub>6</sub> detection system. Its function is to make the detection efficiency  $\varepsilon_\gamma$  proportional to the incident  $\gamma$  ray energy  $E_\gamma$ , as Eq. (3)

$$\varepsilon_\gamma = \sum_{i=1}^n WF_i(E_d)R(E_d, E_\gamma) = \alpha E_\gamma \quad (3)$$

where  $\alpha$  is the constant parameter,  $R$  is the detector response function,  $E_d$  is the energy bin of pulse height spectrum, and WF is the weighting function, which can be approximated by a 5<sup>th</sup> polynomial function. The polynomial coefficients are obtained with a minimum least-squares fit to the the detector response for 27 different monoenergetic  $\gamma$  rays from 0.1 MeV to 10 MeV simulated by the GEANT4 code [46], taking into account the detailed model of the detection systems and the sample.

The background consists of two components, sample-independent and sample-dependent ones. The former is evaluated by the empty sample runs under the same experimental conditions. The sample-dependent background is mainly induced by in-beam  $\gamma$  rays and scattered neutrons on the sample. Their contributions were determined by measurements with a  $^{nat}Pb$  sample and parameterized as eq.(4).

$$B(E_n) = f_\gamma B_\gamma(E_n) + f_n B_n(E_n) \quad (4)$$

where the  $B_\gamma$  and  $B_n$  denote the background contribution of the in-beam gamma rays and scattered neutrons, respectively, and can be formulated as eqs. (5-6).

$$B_\gamma(E_n) = b \times e^{-c/\sqrt{E_n}} + d \times e^{-e \times \sqrt{E_n}} + f \quad (5)$$

$$B_n(E_n) = \frac{a}{\sqrt{E_n}} \quad (6)$$

In order to normalize these background components,  $B_\gamma$  and  $B_n$ , dedicated runs with the  $^{181}\text{Ta}$  and  $^{59}\text{Co}$  neutron filters were performed. Fig. 2 shows the energy spectrum obtained from the  $^{159}\text{Tb}$  with filters and background components. The normalization factors  $f_n$  and  $f_\gamma$  for  $B_n$  and  $B_\gamma$  components were obtained by matching the dips of the filtered spectra. The effect of the filters on in-beam gamma rays and neutrons is evaluated by considering the neutron flux and energy distribution of in-beam gamma rays. The neutron and gamma energy spectra of Back-n are sampled for the incident particle energy spectra using GEANT4 code to simulate with and without filters, and the counts of scattered neutrons and gamma are recorded at the detector position [33]. The reduced neutron and gamma attenuation factors are 0.92 and 0.68, respectively, and are used for corrections to  $f_n$  and  $f_\gamma$ .

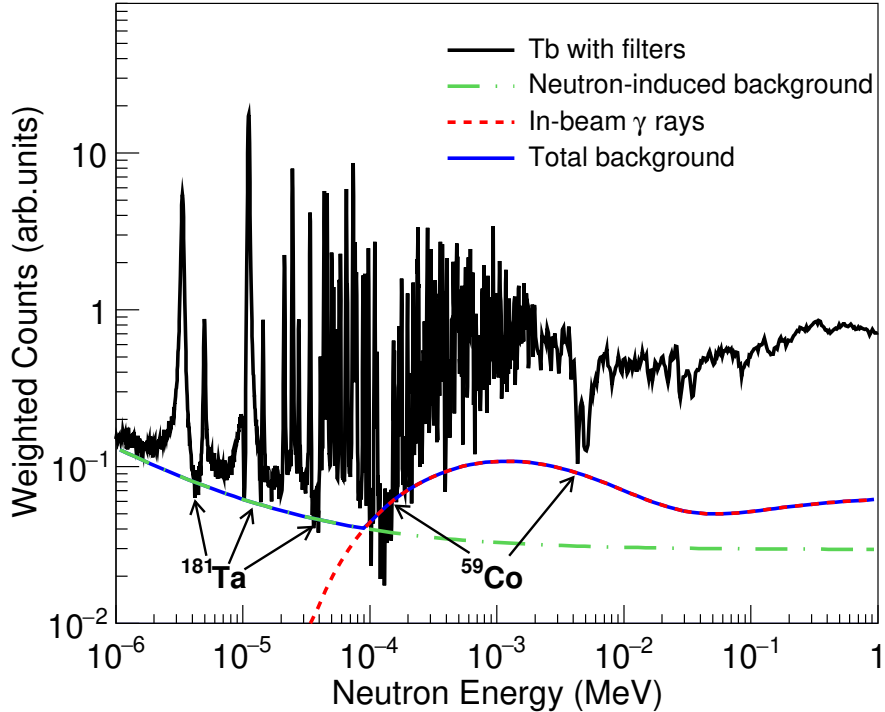


FIG. 2: (color online)  $^{159}\text{Tb}(n, \gamma)$  capture yield with filters and background components are shown as a function of neutron energy. Black and blue solid lines indicate the  $^{159}\text{Tb}$  sample with  $^{181}\text{Ta} + ^{59}\text{Co}$  neutron filters and total background which is made of scattered neutrons (green dash-dotted lines) and in-beam  $\gamma$  rays (red dashed lines).

The resonance parameters (i.e., the radiative width  $\Gamma_\gamma$  and the neutron width  $\Gamma_n$ ) are extracted using the R-matrix code SAMMY [47] to fit the experimental capture yields of  $^{159}\text{Tb}(n, \gamma)$  in the resonance region up to 1.2 keV with the JEFF-3.3 [48] evaluated data as initial values. The code includes the experimental conditions, such as sample composition, multiple scattering, neutron self-shielding, and the Doppler effect at room temperature. The energy-dependent parameterized resolution function of the Back-n facility [49] is used to broaden the resonance peaks. The measured capture yields together with the SAMMY fits in neutron energy ranges below 100 eV are shown in Fig. 3. Good agreements were observed between present data and SAMMY fits both in the resonance energy and shape. The resonance parameters obtained in this work are compared with those from JEFF-3.3 evaluations given in Appendix A. The experimental capture resonance parameters show substantial agreement with the JEFF-3.3 evaluations in the energy range below 100 eV. However, differences are noted in the energy range between 100 eV and 1.2 keV, which is attributed to the degradation of the experimental resolution of the Back-n facility in this measurement. Average resonance parameters (such as the average level spacing, the neutron strength functions, the average radiation widths) are determined by fitting the measured average capture cross section data in the energy range between 2 keV and 200 keV with the code FITACS [50], implemented in SAMMY. The resonance parameters given by Mughabghab [51] are used for initial values in the fitting procedure and the average level spacing is specified as 3.78 eV [51]. The results obtained from the FITACS fit and the recommended data [51, 52] are given in IX.

The measured neutron capture cross section ratio of  $^{159}\text{Tb}$  relative to the standard  $^{197}\text{Au}$  sample is obtained in the neutron energy range of 2 keV to 1 MeV using the same method of Refs. [29, 53]. The absolute cross sections are converted from these ratios using the gold data of JEFF-3.3 evaluations. In Fig. 4, the experimental  $^{159}\text{Tb}(n, \gamma)$  cross section and TALYS-1.9 [54] calculation result of this work are compared with the available measured data in literature [11–16] and evaluated data in libraries JEFF-3.3 [48], ENDF/B-VIII.0 [52]. As illustrated, the present experimental results are in good agreement with the data from TALYS-1.9, Bokhovko et al. [16], and Ohkubo et al. [15] in the overlapping energy regions. The cross section of JEFF-3.3 and Mizumoto et al. [14] are best fitted by the present data below 400 keV neutron energy and slightly larger above 400 keV. On the other hand, the data of Block et al. [11], Gibbons et al. [12], Lépine et al. [13] and ENDF/B-VIII.0 library are significantly overestimated result of this work.

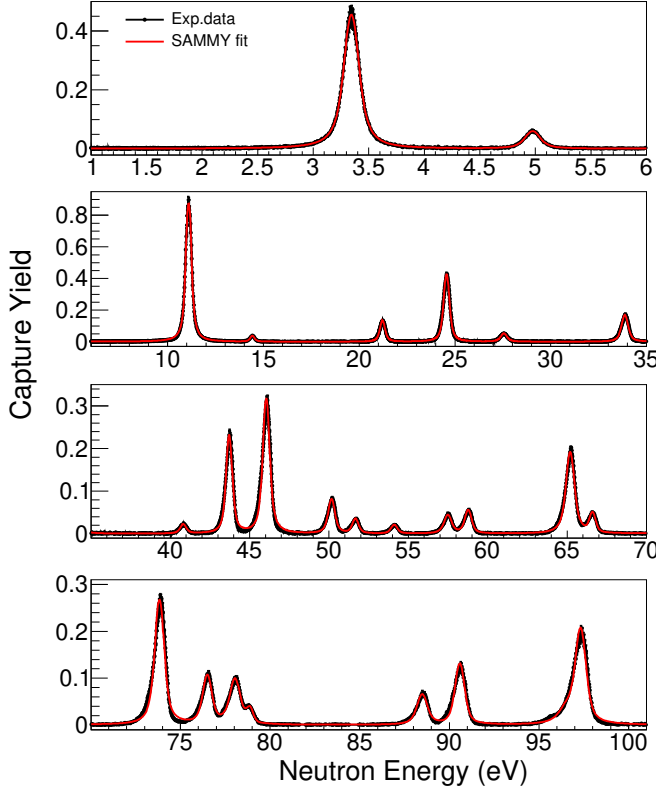


FIG. 3: (color online) The SAMMY fits to the experimental capture yields of  $^{159}\text{Tb} (n, \gamma)$ .

The Maxwellian-averaged cross sections (MACS) for stellar temperature can be calculated from the neutron capture cross sections using the formula (7) [23, 30]:

$$MACS = \frac{2}{\sqrt{\pi}(kT)^2} \int_0^\infty \sigma(E) E e^{-E/kT} dE \quad (7)$$

where  $kT$  is stellar temperature,  $\sigma(E)$  is the neutron capture cross section,  $E$  is the neutron energy.

TABLE II: The contributions from JEFF-3.3 evaluated data to present MACS.

kT (keV)	5	10	20	30	40	50	60	70	80	100
Ratio (%)	10.0	4.0	1.5	0.85	0.56	0.41	0.32	0.28	0.21	0.15

For  $^{159}\text{Tb}(n, \gamma)$ , the present MACS are determined using three parts of cross sections from 1 eV to 1 MeV energy range. The first part, shown in Fig. 5(a), is the cross sections reconstructed from the SAMMY fits to the present measured neutron capture yield in the resolved resonance region below 100 eV. The second part, shown in Fig. 5(b), is derived from the JEFF-3.3 evaluated cross section data between 100 eV and 2 keV since the resonance parameters obtained in this study are not sufficiently reliable due to the degradation of the experimental resolution. The JEFF-3.3

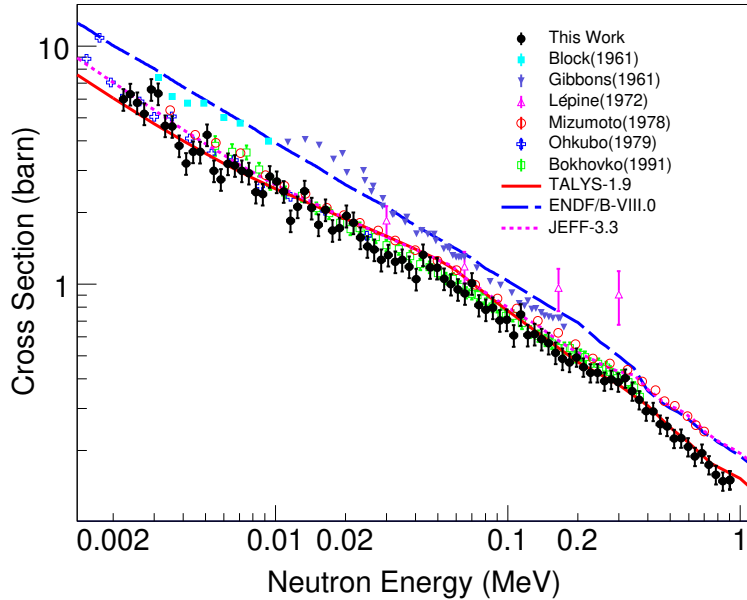


FIG. 4: (color online) Comparisons of the measured neutron capture cross section on  $^{159}\text{Tb}$  of this work (black full circles) with previous measurements [11–16] (symbols), evaluations [48, 52] (dashed lines) and TALYS-1.9 calculations [54] in the 2 keV to 1 MeV energy region.

data contributions to the whole MACS are found in Table II. As we can see, this component cannot be ignored in the current study of s-process nucleosynthesis. The last part is provided by the present experimental cross sections relative to the gold standard over the energy range of 2 keV to 1 MeV as shown in Fig. 5(c).

The result of this work at  $kT = 30$  keV is compared with previous experiments, theoretical calculations, and recommended data from KADoNiS database in Table III. The MACS recommended data from KADoNiS-v0.3 and the calculations of TALYS-1.9 code agree with the present measured data less than 4%. The values from the recent activation measurement of Praena et al. [18], and the earlier data of Allen et al. [55], Lépine et al. [13] are relatively larger than the present result, whereas the results of Bokhovko et al. [16] and NON-SMOKER [58] are smaller. Theoretical calculations from MOST 2002 [57] and MOST 2005 [56] are obviously overestimated and underestimated by 89% and 28%, respectively, compared to the present data.

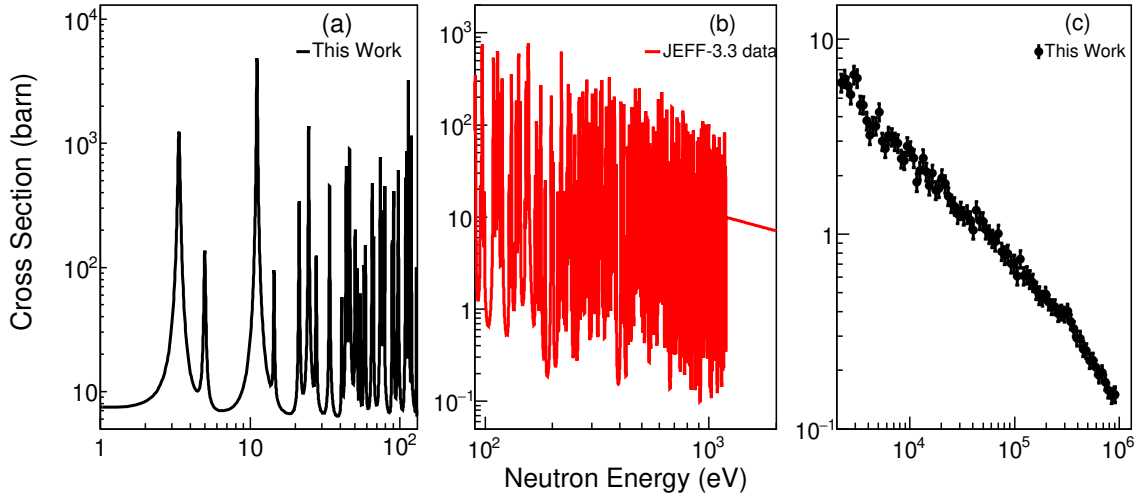


FIG. 5: (color online) The  $^{159}\text{Tb}(n, \gamma)$  cross sections used in the calculation of present MACS.

The MACS values are better to be known as a function of thermal energies between a few to hundred keV at the

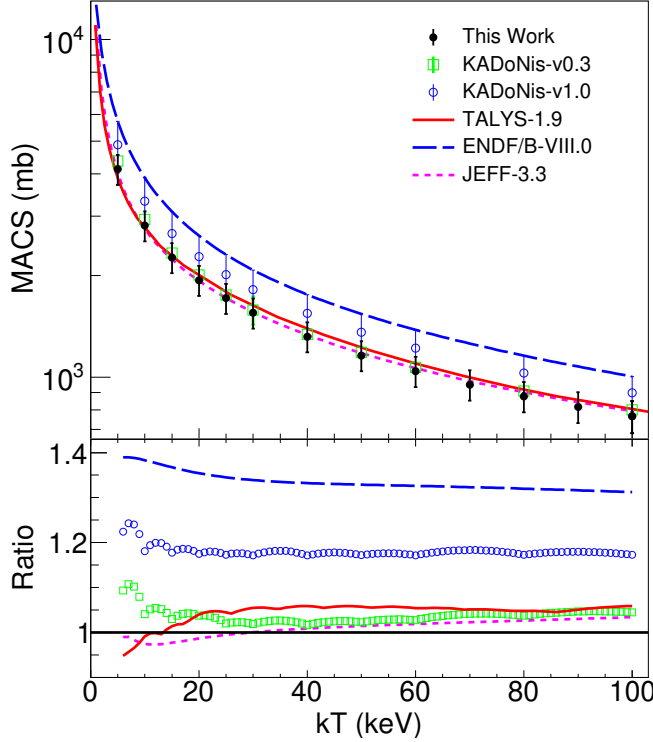


FIG. 6: (color online) (top) The MACS of  $^{159}\text{Tb}(n, \gamma)$  and (bottom) the ratios between present experimental data and others [17, 19, 48, 52].

TABLE III: The present MACS (in mb) of  $^{159}\text{Tb}(n, \gamma)$  at  $kT = 30$  keV compared to past experiments, calculations and evaluations.

	$1560 \pm 160$	KADoNis-v0.3 [17]	$1580 \pm 150$	KADoNis-v1.0 [19]	$1817 \pm 258$
Praena 2014 [18]	$2166 \pm 181$	Bokhovko 1992 [16]	$1471 \pm 66$	Lépine 1972 [13]	$1850 \pm 250$
Allen 1971 [55]	$2200 \pm 200$	MOST 2005 [56]	1116	MOST 2002 [57]	2949
NON-SMOKER [58]	1427	TALYS-1.9 [54]	1628		

TABLE IV: The derived MACS for  $^{159}\text{Tb}(n, \gamma)$  in mb.

$kT(\text{keV})$	This work	KADoNis-v0.3 [17]	KADoNis-v1.0 [19]	TALYS-1.9 [54]	ENDF/B-VIII.0 [52]	JEFF-3.3 [48]
5	$4131 \pm 421$	4365	$4875 \pm 851$	3892	5726	4028
10	$2814 \pm 287$	2930	$3323 \pm 573$	2790	3893	2750
15	$2262 \pm 231$	2330	$2664 \pm 431$	2294	3092	2232
20	$1937 \pm 198$	2010	$2276 \pm 348$	2014	2623	1927
25	$1715 \pm 175$	1750	$2012 \pm 295$	1792	2307	1716
30	$1551 \pm 158$	$1580 \pm 150$	$1817 \pm 258$	1635	2076	1559
40	$1318 \pm 134$	1340	$1544 \pm 211$	1395	1756	1334
50	$1159 \pm 118$	1185	$1358 \pm 181$	1225	1540	1178
60	$1041 \pm 106$	1070	$1220 \pm 159$	1098	1381	1063
80	$877 \pm 91$	910	$1029 \pm 128$	920	1158	902
100	$766 \pm 82$	800	$898 \pm 106$	811	1005	794

various s-process sites. For completeness, the comparisons of the experimental MACS and the TALYS-1.9 calculation result of this work to the recommended data of KADoNis and evaluation libraries for stellar thermal energy from

5 to 100 keV are shown in Fig. 6 and Table IV. On top panel: the black full circles and red solid line denote the present measured data and TALYS-1.9 calculation, respectively; the open green squares and blue circles indicate KADoNis-v0.3 and KADoNis-v1.0 recommended data; the blue dashed line and pink dotted line refer to calculated MACS by using the evaluated cross section data of ENDF/B-VIII.0 and JEFF-3.3 libraries. On bottom panel: the ratios of the measured MACS to those from KADoNis-v0.3 (green open squares), KADoNis-v1.0 (blue open circles), ENDF/B-VIII.0 (blue dashed line), TALYS-1.9 (red solid line), and JEFF-3.3 (pink dotted line) data; Black solid line corresponds to ratio 1. Our measured MACS data is well reproduced by the TALYS-1.9 calculation and the JEFF-3.3 evaluation less than 5% for the entire thermal energies studied. While, the present MACS is significantly smaller than those of ENDF/B-VIII.0 evaluation by 30%–40%. It should be noted that, the present experimental MACS is smaller than KADoNiS-v0.3 data by about 3%–11% and 4% for the energy region  $kT < 20$  keV and  $20 \text{ keV} < kT < 100$  keV, respectively. MACS data derived from KADoNis-v1.0 is larger about 15%–25% than the values of this work in the whole energy range.

The total experimental uncertainties of MACS include statistical and systematic contributions as shown in Table V. The statistical uncertainty is less than 1% below 100 eV and less than 5% between 2 keV and 1 MeV. The systematic uncertainties are due to neutron flux (4.5% below 150 keV and 8.0% above 150 keV), saturated resonance peak normalization (1%), background subtraction with filters (8.6%), flight path (0.08%, neglected), PHWT calculation (3%) and sample impurity (0.01%). Additionally, the contributions from neutron inelastic to the present MACS are included at different stellar temperatures as shown in Table VI, which cannot be eliminated in the present experiment.

TABLE V: Systematic uncertainties of MACS  $^{159}\text{Tb}$  ( $n, \gamma$ ) cross sections.

Source	Uncertainty(%)
Neutron flux ( $< 150$ keV; $> 150$ keV)	4.5; 8.0
Pulse height weighting functions	3.0
Background subtraction with filters	8.6
Normalization factor	1.0
flight path	0.08
Sample impurities	0.01
Total (without inelastic contribution)	10.2;12.2

TABLE VI: The contributions from neutron inelastic to present MACS.

kT (keV)	5	10	20	30	40	50	60	70	80	100
Ratio (%)	$10^{-21}$	$10^{-11}$	$10^{-5}$	$10^{-3}$	$10^{-2}$	0.21	0.68	1.61	3.11	7.90

The astrophysical reaction rates at a given thermal temperature can be numerically calculated from corresponding MACS as eq.(8):

$$N_A < \sigma \nu > (kT) = N_A \times MACS \times \nu \quad (8)$$

where  $N_A$  is the Avogadro number, MACS is defined by Equation (7),  $\nu = \sqrt{2kT/\mu}$  is the mean thermal velocity. The  $^{159}\text{Tb}(n, \gamma)$  rate of this work is fitted as a function of temperature  $T_9$  (in unit of  $10^9$  K) with the standard form of REACLIB:

$$N_A < \sigma \nu >_{(n, \gamma)} = \exp(16.7928 + 0.0115T_9^{-1} - 1.1836T_9^{-1/3} + 4.0069T_9^{1/3} - 0.5127T_9 + 0.03145T_9^{5/3} - 1.3577 \ln T_9) \quad (9)$$

with the fitting errors are less than 1% in the range from  $T_9 = 0.02$  to  $T_9 = 10$ .

#### IV. ASTROPHYSICAL IMPLICATIONS

In TP-AGB stars, the  $^{13}\text{C}$  pocket is formed following the third dredge-up (TDU) via  $^{12}\text{C}(\text{p}, \gamma)^{13}\text{N}(\beta^+ \nu)^{13}\text{C}$  and generate neutrons by reaction  $^{13}\text{C}(\alpha, n)$  that trigger the s-process [59–61]. The impact of  $^{159}\text{Tb}$  stellar neutron capture cross sections on main s-process nucleosynthesis was investigated using the stellar evolution code MESA [62]. The stellar structure evolution and the s-process nucleosynthesis are computed with the MESA *star* and *net* modules separately, hence they requiring less computing time and resources. A low mass star with initial mass  $2M_\odot$  and

metallicity  $Z = 0.01$  evolved from the pre-main sequence to near the end of the TP-AGB phase with nuclear network agb.net. In the  $^{13}\text{C}$  pocket formed after the 3rd TDU episodes, the temperature varies within  $5.5\text{--}8.9 \times 10^7$  K and the density increase from  $96.0 \text{ g/cm}^3$  to  $7.7 \times 10^3 \text{ g/cm}^3$  during the whole interpulse phase.

To treat the s-process, detailed nucleosynthesis calculations were performed with MESA *net* module. The network include 775 isotopes and 7344 reactions, and the temperature, density and light nuclei initial abundance are extracted from the  $^{13}\text{C}$  pocket of the precalculated stellar structure. The reaction rates corresponding to all proton,  $\alpha$ ,  $\beta$ -decay, and neutron capture are provided by JINA REACLIB data tables, based on the 2017 updated version of the compilation by Cyburt et al. [63]. In addition, the initial element abundances are taken from Lodders et al. [64] for both structure and nucleosynthesis simulations.

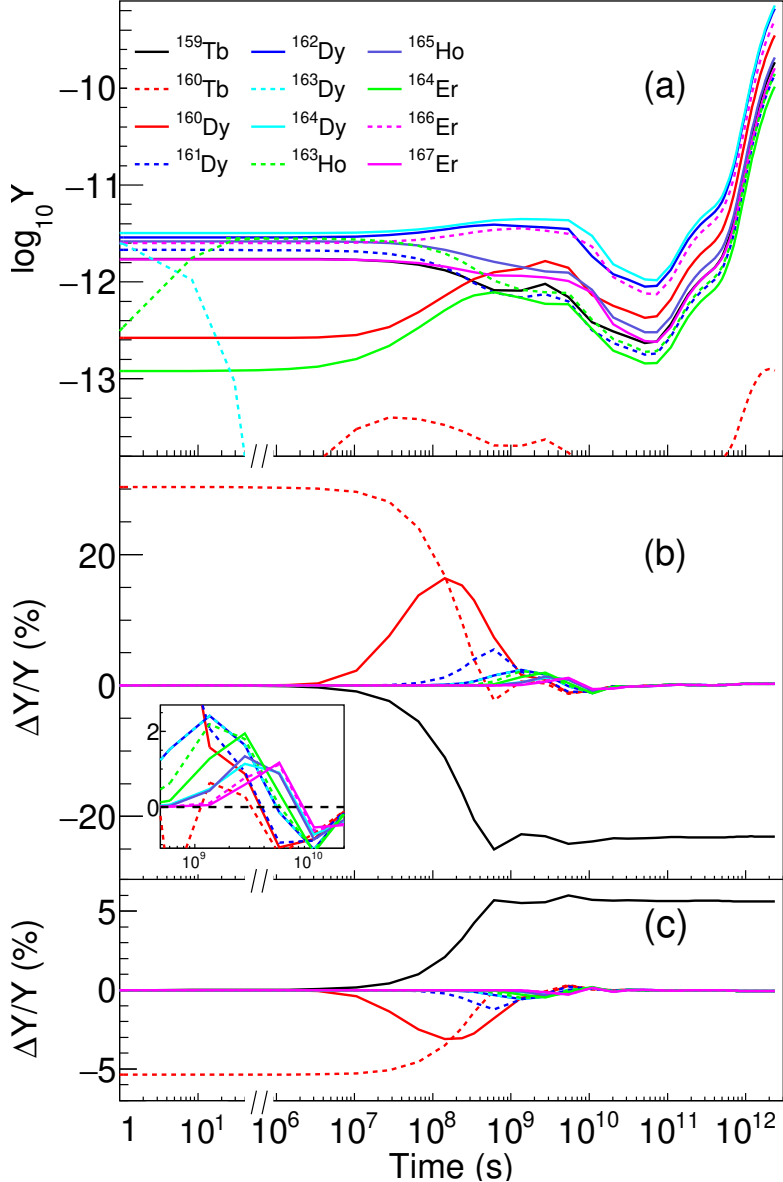


FIG. 7: (color online) (Top) Time evolution of nuclear abundances on the test trajectory with  $T = 8.9 \times 10^7$  K and  $\rho = 7.7 \times 10^3 \text{ g/cm}^3$ . (Middle) The abundance differences between the default case of the JINA REACLIB rate for  $^{159}\text{Tb}(n, \gamma)^{160}\text{Tb}$ , which is derived from KADoNiS-v0.3, and the case of ENDF/B-VIII.0. (Bottom) Same physical quantities as in Middle one but the reaction rates of this work instead of ENDF/B-VIII.0 data are used in calculations.

The sensitivity of nuclear yields is evaluated to the reaction rate of  $^{159}\text{Tb}(n, \gamma)^{160}\text{Tb}$ . Fig. 7(a) shows the time evolution of the abundances of nuclides around  $A \approx 160$  along the s-process reaction path at constant temperature ( $T = 8.9 \times 10^7$  K) and density ( $\rho = 7.7 \times 10^3 \text{ g/cm}^3$ ) with the default case of the JINA REACLIB rate for  $^{159}\text{Tb}(n, \gamma)^{160}\text{Tb}$ , which is derived from the KADoNiS-v0.3 database. The abundance of  $^{163}\text{Dy}$ , which has a half-live of about

50 days in stellar environment [65], decreases rapidly due to the considering  $\beta$ -decay process to  $^{163}\text{Ho}$ . The abundances of seed nuclei with initial values around  $A \approx 160$  decreased significantly by neutron capture reactions before evolving to  $7 \times 10^{10}$  s because of the s-process flow from the dominant seed nuclei  $^{56}\text{Fe}$  not yet overcomes the first s-process peak nuclei Sr and Ba, which act as the bottle necks in the reaction flow. On the other hand, the abundances of  $^{160}\text{Dy}$  and  $^{164}\text{Er}$  increased obviously with the depletion of  $^{160}\text{Tb}$  and  $^{163}\text{Ho}$  from about  $10^7$ – $4 \times 10^9$  s. Then, the productions of all nuclides around  $A \approx 160$  increase continuously up to 2–3 orders larger than initial values at the end of interpulse. Fig.7(b) shows the abundance changes between the KADoNiS-v0.3 and the ENDF/B-VIII.0 rate of  $^{159}\text{Tb}(n, \gamma)^{160}\text{Tb}$  used in the network calculations. In this case, the data of KADoNiS-v0.3 is smaller about by 40% than the one of ENDF/B-VIII.0. The abundances of  $^{159,160}\text{Tb}$ ,  $^{160,161}\text{Dy}$  noticeably are affected by the uncertainty of cross section of the  $^{159}\text{Tb}(n, \gamma)^{160}\text{Tb}$  reaction. While, this propagation effects are less important for those nuclei heavier from  $^{159}\text{Tb}$ . This trend is caused by achieving s-process reaction flow equilibriums [1, 66, 67] due to the high neutron fluence in the  $^{13}\text{C}$  pocket. Fig.7(c) shows the same physical quantities as in Fig.7(b) but with the  $^{159}\text{Tb}(n, \gamma)^{160}\text{Tb}$  rate of this work instead of the ENDF/B-VIII.0 data in calculations. As shown in the figure, the changes of abundances are much smaller than those of Fig.7(b) because of good agreement between two rates within 5%.

## V. SUMMARY

We measured  $^{159}\text{Tb}(n, \gamma)$  cross sections up to 1 MeV neutron energy by TOF method using the  $\text{C}_6\text{D}_6$  detectors at the CSNS Back-n facility. Resonance capture kernels are determined from 1 eV to 1.2 keV by analyzing the measured data with the R-matrix code SAMMY. The cross sections are obtained relative to the gold standard over the energy range of 2 keV to 1 MeV and agree well with the TALYS-1.9 theoretical calculations and the JEFF-3.3 evaluation library within the experimental errors. On the other hand, the ENDF/B-VIII.0 evaluated cross section significantly overestimated to those of the present study. Maxwellian-averaged neutron capture cross sections (MACS) extracted from the present  $(n, \gamma)$  data are in good agreement with the data of JEFF-3.3 and KADoNiS-v0.3 [17] within 5% and 3%–11% of discrepancies in the whole energy range, respectively. However, the data of ENDF/B-VIII.0 and KADoNiS-v1.0 [19] are significantly overestimated to the present experimental results by 40% and 20%. The sensitivity analysis of  $^{159}\text{Tb}(n, \gamma)^{160}\text{Tb}$  reaction rate is investigated for the stellar evolution and nucleosynthesis of the  $2M_{\odot}$  star model using the MESA code. Significant changes in abundances of  $^{159,160}\text{Tb}$ ,  $^{160,161}\text{Dy}$  are observed by comparing the stellar reaction rates of  $^{159}\text{Tb}(n, \gamma)^{160}\text{Tb}$  between KADoNiS-v0.3, this work and ENDF/B-VIII.0 evaluation. The present results show very small propagation to the more heavier elements for changing the rate of  $^{159}\text{Tb}(n, \gamma)^{160}\text{Tb}$  because of the establishment of a reaction flow equilibrium between the s-process main component nuclei.

## ACKNOWLEDGMENTS

This work was supported by the National Natural Science Foundation of China (Grants No. U2032146, 11865010, 12175152, 11765014 and 11609053), Natural Science Foundation of Inner Mongolia (Grants No. 2019JQ01 and 2018MS01009) and the Program for Young Talents of Science and Technology in Universities of Inner Mongolia Autonomous Region (NJT23109). We also thank the efforts of the CSNS Back-n collaboration.

## Appendix A. Resonance Parameters

The resonance parameters obtained from fitting the measured capture yield of  $^{159}\text{Tb}(n, \gamma)$  with R-matrix code SAMMY are compared with those from JEFF-3.3 evaluations in Tables VII and VIII. In the energy region from 100 eV to 2 keV, the resonance parameters are not sufficiently reliable due to the worsening of the experimental resolution at Back-n facility. Therefore, only the resonance energies  $E_R$  and capture kernels  $k$  ( $k = g\Gamma_n\Gamma_\gamma/(\Gamma_n + \Gamma_\gamma)$ ,  $g$  is the statistical factor) in this energy range are listed in VIII. Average resonance parameters, namely the average level spacing  $D_l$ , the neutron strength function  $S_l$  and the average radiation width  $\langle \Gamma_\gamma \rangle_l$ , obtained in this work and the recommended data are listed in Table IX. The uncertainties in Tables of this work are from the fitting procedures.

**Table VII** Resonance parameters up to 100 eV neutron energy for  $^{159}\text{Tb}(n, \gamma)$  reaction.

J	This work				JEFF-3.3			
	$E_R$ [eV]	$\Gamma_n$ [meV]	$\Gamma_g$ [meV]	k	$E_R$ [eV]	$\Gamma_n$ [meV]	$\Gamma_g$ [meV]	k
2	$3.34 \pm 0.03$	$0.34 \pm 0.02$	$102.12 \pm 0.06$	$0.21 \pm 0.01$	3.360	0.34	103.00	0.21
1	$4.97 \pm 0.13$	$0.07 \pm 0.05$	$100.58 \pm 0.04$	$0.03 \pm 0.01$	4.990	0.08	103.00	0.03
2	$11.04 \pm 0.03$	$4.97 \pm 0.15$	$105.45 \pm 0.02$	$2.97 \pm 0.10$	11.130	7.69	99.00	4.46
1	$14.40 \pm 0.30$	$0.12 \pm 0.04$	$95.46 \pm 0.08$	$0.04 \pm 0.01$	14.500	0.19	105.00	0.07
2	$21.19 \pm 0.13$	$1.33 \pm 0.18$	$105.24 \pm 0.31$	$0.82 \pm 0.07$	21.190	1.14	102.00	0.71
2	$24.53 \pm 0.07$	$3.77 \pm 0.16$	$128.35 \pm 1.40$	$2.29 \pm 0.09$	24.520	5.32	116.00	3.18
2	$27.55 \pm 0.34$	$0.48 \pm 0.09$	$95.68 \pm 0.85$	$0.30 \pm 0.05$	27.510	0.83	102.00	0.52
2	$33.83 \pm 0.12$	$3.56 \pm 0.58$	$105.67 \pm 0.28$	$2.15 \pm 0.12$	33.810	2.61	98.00	1.59
1	$40.81 \pm 0.63$	$0.55 \pm 0.18$	$105.78 \pm 1.73$	$0.21 \pm 0.06$	40.740	0.84	101.00	0.31
2	$43.69 \pm 0.13$	$4.33 \pm 0.28$	$103.54 \pm 1.25$	$2.60 \pm 0.14$	43.630	5.90	97.00	3.48
2	$46.04 \pm 0.14$	$7.62 \pm 0.52$	$113.48 \pm 1.29$	$4.46 \pm 0.23$	45.990	13.94	109.00	7.72
2	$50.16 \pm 0.24$	$1.80 \pm 0.12$	$102.86 \pm 0.61$	$1.11 \pm 0.10$	50.070	1.91	96.00	1.17
2	$51.61 \pm 0.38$	$1.13 \pm 0.24$	$98.15 \pm 1.02$	$0.70 \pm 0.12$	51.550	0.84	96.00	0.52
1	$54.08 \pm 0.53$	$0.43 \pm 0.12$	$85.21 \pm 1.14$	$0.16 \pm 0.04$	53.990	0.83	78.00	0.31
1	$57.45 \pm 0.36$	$2.09 \pm 0.38$	$102.48 \pm 1.00$	$0.77 \pm 0.10$	57.350	2.20	99.00	0.81
2	$58.77 \pm 0.29$	$1.38 \pm 0.22$	$98.65 \pm 0.79$	$0.85 \pm 0.10$	58.630	1.59	96.00	0.98
2	$65.17 \pm 0.18$	$7.90 \pm 0.54$	$98.25 \pm 1.44$	$4.57 \pm 0.25$	65.091	12.61	96.00	6.97
1	$66.56 \pm 0.39$	$1.82 \pm 0.51$	$93.22 \pm 1.10$	$0.67 \pm 0.13$	66.484	3.52	98.00	1.27
1	$73.83 \pm 0.14$	$13.02 \pm 0.82$	$102.15 \pm 1.30$	$4.33 \pm 0.19$	73.665	19.09	98.00	5.99
1	$76.45 \pm 0.29$	$7.35 \pm 0.98$	$116.67 \pm 2.79$	$2.59 \pm 0.27$	76.318	6.92	108.00	2.44
1	$77.98 \pm 0.37$	$5.03 \pm 0.88$	$102.14 \pm 2.22$	$1.80 \pm 0.24$	77.773	7.25	96.00	2.53
1	$78.80 \pm 0.67$	$1.06 \pm 0.62$	$95.15 \pm 2.00$	$0.39 \pm 0.18$	78.598	2.68	85.00	0.97
2	$88.44 \pm 0.42$	$3.54 \pm 0.66$	$86.62 \pm 1.11$	$2.13 \pm 0.26$	88.240	3.37	70.00	2.01
2	$90.60 \pm 0.33$	$11.72 \pm 1.75$	$105.68 \pm 2.74$	$6.59 \pm 0.67$	90.310	6.84	90.00	3.97
1	$97.24 \pm 0.31$	$24.37 \pm 5.12$	$118.76 \pm 4.77$	$7.58 \pm 0.93$	97.004	38.21	101.00	10.40

**Table VIII** The resonance energies and kernels in this work are compared with the JEFF-3.3 from 100 eV to 1.2 keV.

This work				JEFF-3.3			
$E_R$ [eV]	$k$	$E_R$ [eV]	$k$	$E_R$ [eV]	$k$	$E_R$ [eV]	$k$
109.24±0.22	8.24±0.34	111.56±0.27	3.04±0.217	108.98	8.19	111.26	2.76
113.89±0.26	6.79±0.472	115.73±0.32	2.25±0.173	113.61	10.66	115.41	3.62
118.83±0.28	2.45±0.225	128.46±0.25	0.63±0.0465	119.06	5.63	128.13	0.53
137.28±0.62	1.28±0.267	138.25±0.45	2.96±0.366	137.43	1.45	137.89	3.57
141.47±0.26	14.80±2.91	143.69±0.26	2.55±0.942	141.16	13.63	143.3	3.98
152.90±0.24	9.67±0.747	155.95±0.28	6.08±0.479	152.52	7.38	155.43	13.48
167.96±0.40	0.83±0.0827	170.13±0.30	3.50±0.258	167.47	0.77	169.63	3.1
173.03±0.38	2.07±0.144	177.21±0.40	6.40±0.447	172.56	1.5	177.3	8.37
186.00±0.53	0.47±0.043	197.78±0.44	6.73±0.414	185.42	0.8	197.36	7.45
200.24±0.48	1.07±0.135	201.84±0.02	0.83±0.439	199.60	1.81	201.37	1.39
211.15±0.54	0.73±0.0579	219.61±0.39	12.13±0.893	210.80	0.71	218.99	28.42
226.33±0.78	0.97±0.109	229.15±1.60	0.41±0.102	225.90	0.79	228.4	0.38
235.67±0.57	15.15±0.928	239.34±0.43	14.12±1.43	235.10	13.25	238.6	11.02
242.17±0.45	5.41±0.516	245.28±0.16	0.15±0.0367	241.43	5.98	244.4	0.47
251.93±0.61	1.90±0.18	254.75±0.58	0.79±0.0953	251.18	3.77	254.1	1.23
263.24±0.71	6.89±0.519	269.05±0.61	5.16±0.329	262.90	10.68	268.39	4.15
273.83±0.58	7.15±0.557	280.05±0.96	1.82±0.341	273.37	13.24	279.8	1.22
281.86±0.69	6.61±0.803	284.77±0.53	17.03±3.04	281.3	6.71	284.14	20.96
290.57±0.59	3.68±0.362	301.43±0.61	16.92±1.03	290.12	6.51	300.76	14.29
306.22±0.65	10.40±0.813	312.88±0.65	14.52±0.968	305.49	9.36	312.11	17.66
316.27±0.99	1.73±0.322	324.12±1.12	8.25±1.21	315.29	2.12	323.1	6.83
326.58±1.26	10.49±2.57	329.02±0.71	22.49±5.41	325.54	5.41	328.01	19.12
332.86±0.64	21.90±2.48	337.82±0.56	0.13±0.0832	331.94	24.1	336.92	1.08
340.49±0.59	0.18±0.0908	346.16±2.18	12.39±2.49	339.43	0.95	345.28	4.3
348.50±1.58	10.67±3.24	350.83±1.34	4.58±1.19	347.46	13.32	349.88	5.62

continued on next page

**Table VIII**(continued)

This work				JEFF-3.3			
$E_R$ [eV]	$k$	$E_R$ [eV]	$k$	$E_R$ [eV]	$k$	$E_R$ [eV]	$k$
358.90±0.78	39.25±2.52	367.32±1.40	10.58±1.54	358.70	29.9	366.32	6.69
370.07±1.79	6.75±2.2	372.77±0.88	22.02±3.26	368.64	3.67	371.81	16.48
375.37±1.21	13.50±2.54	379.40±0.82	18.89±1.62	374.14	11.13	378.16	20.49
385.42±0.82	2.83±0.345	403.20±1.61	8.00±1.55	384.80	3.4	404.5	18.3
409.99±1.22	4.82±0.868	429.98±2.88	0.57±0.218	409.02	6.25	429.1	0.64
433.16±1.11	6.32±0.691	440.26±2.65	10.52±2.66	432.24	6.29	439.96	11.49
442.32±2.07	7.75±3.04	444.97±2.60	5.81±1.58	442.60	9.39	444.45	3.42
451.34±4.06	5.19±2.31	453.39±1.91	10.79±3.73	450.98	1.92	452.8	15.47
455.15±2.46	8.02±3.1	458.69±1.06	9.02±1.2	453.10	3.7	457.7	13.7
463.83±0.02	0.26±0.25	466.15±2.81	2.19±0.846	463.32	1.13	467.87	33.72
475.37±1.47	22.85±2.47	482.73±2.17	3.49±4.38	474.00	12.53	482.07	27.77
489.83±0.87	31.60±5.5	495.58±2.18	10.62±2.69	488.52	37.82	493.97	12.96
499.21±3.03	8.99±2.87	504.15±1.35	13.43±1.6	497.77	6.55	502.96	14.56
511.47±1.65	4.77±0.695	518.43±3.54	5.23±1.87	510.06	12.95	517.37	3.68
521.88±1.58	25.19±2.91	529.19±1.47	17.40±2.07	520.78	21.44	527.79	19.16
533.60±0.88	14.93±2.81	544.84±2.70	4.07±1.42	532.83	18.45	544.5	9.64
547.17±2.92	5.38±1.75	553.36±2.92	8.91±1.85	546.32	1.9	551.8	8.88
558.28±4.99	4.80±2.44	561.60±3.53	12.98±4.92	557.02	7.7	560.47	8.11
566.04±2.01	33.91±5.72	571.47±2.78	10.74±2.55	564.71	16.34	569.73	12.92
576.44±2.79	2.97±1.02	578.42±3.35	4.06±1.49	575.70	4.59	577.39	2.77
581.01±2.24	5.56±1.32	592.31±3.82	23.21±6.52	579.68	14.88	592.39	17.81
594.83±2.48	24.69±8.43	597.47±3.25	16.48±6.58	593.60	35.43	597.52	19.04
600.41±2.16	17.77±5.24	603.10±2.68	9.54±3.21	600.02	11.05	602.71	13.72
605.90±3.19	4.63±1.68	610.50±3.57	16.60±3.29	605.50	2.31	608.12	8.64
615.81±0.94	27.31±9.28	619.30±2.74	7.33±1.91	615.34	50.31	620.49	11.09
627.47±3.03	9.57±3.67	630.28±3.80	17.25±4.37	627.03	22.74	630.29	8.11
639.30±3.02	11.98±2.34	644.79±3.11	11.45±3.57	637.60	8.15	644.28	7.86
649.11±1.49	23.02±5.35	658.22±3.85	1.07±0.358	648.35	31.82	654.5	2.46
660.53±1.76	4.01±0.684	663.24±1.33	4.11±0.636	659.92	8.03	662.6	5.29

continued on next page

**Table VIII**(continued)

This work				JEFF-3.3			
$E_R$ [eV]	$k$	$E_R$ [eV]	$k$	$E_R$ [eV]	$k$	$E_R$ [eV]	$k$
678.45±2.51	4.75±1.06	681.88±2.86	7.41±2.1	677.70	4.55	682.51	16.06
684.57±2.23	12.86±2.91	687.71±2.97	18.41±4.44	683.60	34.2	686.64	14.48
694.55±4.29	8.90±2.98	702.00±3.12	15.57±3.21	693.48	7.61	700.57	14.2
708.96±2.52	12.70±2.27	720.87±1.91	8.45±2.84	707.47	6.79	719.68	33.22
723.53±0.40	3.99±2.51	727.88±4.88	3.51±1.75	723.08	1.94	726.97	6.11
732.89±2.91	27.50±4.62	740.27±5.74	6.82±2.59	731.75	25.83	738.5	9.01
748.01±3.48	4.48±1.44	750.91±3.58	4.70±1.61	747.32	7.29	751.46	10.19
754.69±3.68	5.91±1.77	767.45±2.14	57.03±7.81	753.90	5.15	765.2	40.77
768.77±6.80	25.42±22.3	783.42±4.63	6.08±2.81	769.80	19.03	782.5	3.92
787.44±2.68	37.04±8.35	790.76±2.32	21.69±5.76	787.70	28.37	793	6.31
802.50±4.95	12.41±3.37	810.17±5.36	10.99±5.99	802.00	23.45	810.2	16.41
814.44±7.91	15.65±6.87	824.44±2.35	35.91±3.31	815.70	5.22	823.9	22.62
837.62±4.69	2.01±0.792	845.01±3.69	39.72±7.69	837.00	3.88	845.3	25.67
849.34±2.22	31.80±6.76	853.81±3.24	19.32±5.49	850.50	26.82	855.9	6.53
859.26±4.33	8.40±3.06	872.33±19.42	3.24±2.78	861.40	8.88	869.8	4.12
876.21±6.60	14.09±5.05	884.20±4.27	25.68±7.24	875.40	5.39	884.7	21.25
896.76±9.85	6.21±5.75	901.55±3.01	25.35±7	896.40	9.01	901.5	24.29
911.67±10.04	7.09±4.4	925.28±2.25	30.40±5.38	921.50	4.86	924.9	32.15
935.80±2.14	138.65±11.8	951.33±3.99	5.43±1.82	936.00	42.09	951.3	17.54
955.25±6.16	2.95±1.56	966.97±2.56	21.96±6.41	955.30	6.37	968.4	10.9
971.69±2.67	21.47±4.59	979.62±3.80	29.03±6.75	972.60	17.65	980.2	29.62
994.59±2.90	42.17±6.68	998.76±5.29	24.14±1.07	995.20	43.79	1000.7	20.79
1005.19±78.01	1.36±0.14	1015.76±77.30	6.81±0.68	1005.00	5.74	1016.2	12.62
1028.42±78.92	1.03±1.03	1036.81±78.88	0.28±0.283	1028.00	6.57	1036.3	17.27
1040.66±79.00	0.04±0.0372	1050.39±79.47	0.06±0.0572	1040.20	23.26	1050	33.11
1057.37±79.81	0.03±0.031	1068.11±79.95	4.79±4.76	1057.00	31.37	1067.7	14.64
1097.87±81.84	0.17±0.173	1105.74±82.28	0.31±0.313	1097.60	24.61	1105.5	17.37
1124.31±83.28	0.93±0.929	1132.41±83.67	0.77±0.77	1124.10	20.15	1132.2	21.64
1142.81±85.02	2.98±0.298	1148.20±84.49	0.89±0.888	1142.70	7.42	1148	21.73

continued on next page

**Table VIII**(continued)

This work				JEFF-3.3			
$E_R$ [eV]	$k$	$E_R$ [eV]	$k$	$E_R$ [eV]	$k$	$E_R$ [eV]	$k$
1157.19±85.48	10.46±10.5	1172.96±135.74	39.86±46.8	1157.00	13.28	1172.8	51.88
1184.70±87.74	4.23±4.21	1192.36±86.92	1.14±1.14	1184.40	17.68	1192.2	15.7

**Table IX** Average resonance parameters of this work and the recommended data from S.F.Mughabghab [51] and ENDF/B-VIII.0 [52].

Parameters	ThisWork	ENDF/B-VIII.0	S.F.Mughabghab
$S_0(10^{-4})$	1.53±0.02	1.207	1.55±0.15
$S_1(10^{-4})$	1.83±0.05	1.480	1.86±0.09
$S_2(10^{-4})$	1.55±0.21	1.090	1.41±0.24
$\langle \Gamma_\gamma \rangle_0$ (eV)	0.098±0.002	0.097	0.101±0.002
$\langle \Gamma_\gamma \rangle_1$ (eV)	0.055±0.003	0.097	0.050±0.004
$\langle \Gamma_\gamma \rangle_2$ (eV)	0.098	0.097	-

\* E-mail at:zsytl@imun.edu.cn

† E-mail at:huangmeirong@imun.edu.cn

- [1] R. Reifarth, C. Lederer, and F. Kappeler, J. Phys. G: Nucl. Part. Phys. **41**, 053101(2014).
- [2] F.-K. Thielemann, *et al.*, Prog. Part. Nuc. Phys. **66** ,346(2011).
- [3] E. Burbidge, G. Burbidge, W. Fowler and F. Hoyle, Rev. Mod. Phys. **29**, 547(1957).
- [4] A. Cameron, Technical Report CRLC41 (Chalk River: Atomic Energy of Canada,Ltd.), 1957.
- [5] M. Arnould, S. Goriely, Phys. Rep. **384** , 1(2003).
- [6] S.E. Woosley, D.H. Hartmann, R.D. Hoffman, and W.C. Haxton, Astrophys. J. **356** , 272(1990).
- [7] S. Bisterzo, *et al.*, Mon. Not. R. Astron. Soc. **418** , 284(2011).
- [8] F. Voss, *et al.*, Phys. Rev. C **59**(2), 1154(1999).
- [9] W. Rapp, *et al.*, Astrophys. J. **653** , 474(2006).
- [10] T. Hayakawa, *et al.*, Astrophys. J. **685** , 1089(2008).
- [11] R.C. Block, *et al.*, in Proceedings of the EANDC Conference on Time of Flight Method, Saclay (European Atomic Energy Community, Brussels, 1961), p. 203.
- [12] J. H. Gibbons, *et al.*, Phys. Bev **122**, 182 (1961).
- [13] J.R.D. Lépine, *et al.*, Nucl. Phys. A **196**, 83(1972).
- [14] M. Mizumoto, R. Macklin, and J. Halperin, Phys. Rev. C **17**, 522(1978).
- [15] M.Ohkubo, and Y. Kawarasaki, J. Nucl. Sci. Technol. **16**, 701(1979).
- [16] M. Bokhovko, *et al.*, Proc. Nucl. Data for Science and Tech. Juelich, Germany (1991).
- [17] I. Dillmann, R. Plag, F. Kappeler, EFNUDAT Fast Neutrons: Scientific workshop on neutron measurements, theory applications, JRC-IRMM, available online:www.kadonis.org
- [18] J. Praena, *et al.*, Nucl. Data Sheets **120** , 205(2014).
- [19] The Karlsruhe Astrophysical Database of Nucleosynthesis in Stars 1.0 (test version), online at <https://exp-astro.de/kadonis1.0/>
- [20] N.Dzysiuk, *et al.*, Nucl. Phys. A **936** , 6(2015).
- [21] C. Jin-Xiang, *et al.*, Nucl. Sci. Tech. **9** , 139(1998).
- [22] C. Guerrero, *et al.*, Phys. Rev. Lett. **125**, 142701(2020).

- [23] C. Lederer-Woods, *et al.*, Phys. Lett. B **790** , 458(2019).
- [24] B.J. McDermott, *et al.* Phys. Rev. C **99** , 055809(2019).
- [25] C. Lederer, *et al.*, Phys. Rev. Lett. **110**, 022501(2013).
- [26] U. Abbondanno, *et al.*, Phys. Rev. Lett. **93(16)**, 161103(2004).
- [27] C.J. Prokop, *et al.*, Phys. Rev. C **99** , 055809(2019).
- [28] O.Roig, *et al.*, Phys. Rev. C **93** , 034602(2016).
- [29] K. Wissak, *et al.*, Phys. Rev. C **73**, 015807(2006).
- [30] K. Wissak, *et al.*, Phys. Rev. C **42(4)**, 1731(1990).
- [31] J. Tang, *et al.*, Chin. Phys. C **45**, 062001(2021).
- [32] J. Tang, *et al.*, Nuclear Science and Techniques **32**, 11(2021).
- [33] J. Ren,*et al.*, Chin. Phys. C **46(4)**, 044002(2022).
- [34] X.X. Li,*et al.*, Phys. Rev. C **104**, 054302(2021).
- [35] J. Ren,*et al.*, Nucl. Instr. and Meth. A **985**, 164703(2021).
- [36] L. Xie,*et al.*, Journal of Instrumentation bf 16, P10029(2021).
- [37] J.L. Tain, *et al.*, Nucl. Instr. and Meth. A **39(sup2)**, 689(2002).
- [38] U. Abbondanno, *et al.*, Nucl. Instr. and Meth. A **521**, 454(2004).
- [39] P. Schillebeeckx, *et al.*, Nucl. Data Sheets **113**, 3054(2012).
- [40] Q. Li, *et al.*, Nucl. Instr. and Meth. A **946**, 162497(2019).
- [41] Y. Chen, *et al.*, Eur. Phys. J. A **55**, 115(2019).
- [42] Q. Wang, *et al.*, Rev. Sci. Instrum. **89**, 013511(2018).
- [43] Rene Brun and Fons Rademakers, Nucl. Inst. Methods. A **389**,81 (1997). See also <https://root.cern/>.
- [44] R.L. Macklin, *et al.*, Nucl. Instrum. Methods **164(1)**, 213 (1979).
- [45] A. Borella, *et al.*, Nucl. Instrum. Methods A **577**, 626 (2007).
- [46] S. Agostinelli, *et al.*, Nucl. Instrum. Methods A **506**, 250 (2003).
- [47] N.M. Larson, Updated users guide for SAMMY: Multilevel R-matrix fits to neutron data using Bayes equations, Report No. ORNL/TM-9179/R8,ENDF-364/R2,Oak Ridge National Laboratory, 2008.
- [48] The Joint Evaluated Fission and Fusion File (JEFF) <https://www.oecd-nea.org/dbdata/JEFF33/>.
- [49] B. Jiang, *et al.*, Nucl. Instrum. Methods A **1013**, 165677 (2021).
- [50] F.H. Froehner, Nucl. Sci. Eng. **103**, 119 (1989).
- [51] S. F. Mughabghab, Atlas of Neutron Resonances 6th Edition: Resonance Parameters and Thermal Cross Sections. (Elsevier 2018).
- [52] D.A. Brown, *et al.*, Nucl. Data Sheets **148**, 1(2018).
- [53] M. Tessler, *et al.*, Phys. Lett. B **751**, 418(2015).
- [54] A.J. Koning, *et al.*, Nucl. Data Sheets **155**, 1(2019).
- [55] B. Allen, J. Gibbons, and R. Macklin, Adv. Nucl. Phys. **4** , 205(1971).
- [56] S. Goriely, Hauser-Feshbach rates for neutron capture reactions (version 8/29/2005), (2005).
- [57] S. Goriely, Hauser-Feshbach rates for neutron capture reactions (version 9/12/2002), (2002).
- [58] T. Rauscher and F.-K. Thielemann, Atomic. Data. Nucl. Data Tables **75** , 1(2000).
- [59] C.E. Rolfs, W.S. Rodney. Cauldrons in the Cosmos. The University of Chicago Press,1988.
- [60] A.I. Karakas, J.C. Lattanzio, Publications of the Astronomical Society of Australia **31**, 62(2014).
- [61] S. Cristallo, *et al.*, Astrophys. J **1**, 696(2009).
- [62] B.Paxton, *et al.*, Astrophys. J. Suppl **192**, 3(2011).
- [63] R.H. Cyburt,*et al.*, Astrophys. J. Suppl **189(1)**, 240(2010).
- [64] K. Lodders. Astrophys. J **591(2)**, 1220(2003).
- [65] K. Takahashi, Phys. Rev. C **36(4)**, 1152(1987).
- [66] F. Kappeler,*et al.*, Rev. Mod. Phys. **83**, 157(2011).
- [67] A. Koloczek, *et al.*, At. Data Nucl. Data Tables **108**, 1(2016)